2550° to 2700°F in air at 0.10 to 1.0 mm Hg.[5] A similar effect of pressure has been found for Sn-Al base coatings on tantalum-base alloys.[7] In this case, volatilization of tin at low pressure destroys the coating and results in premature failure.

The only approach to this problem at present is to allow for degradation effects in the design and use of parts that will operate in low-pressure environments. The performance of eight different coating systems is being characterized as a function of air pressure at this time, and results should be available for use by early 1965.[5]

References

[1] Srp, O. O. and Geyer, N. M., "Protective coating requirements and recent developments," *Proceedings of International Symposium on High Temperature Technology* (Stanford Research Institute, Menlo Park, Calif., September 1963).

[2] Moore, V. S. and Stetson, A. R., "Evaluation of coated refractory metals foils," Aeronautical Systems Div. ASD-TDR 63-4006, Part I (September 1963).

[3] Perkins, R. A., Price, W. L., and Coons, W., "Factors affecting the performance of silicide base coatings on refractory metals," Gordon Research Conferences (July 1963).

[4] Berkowitz, J. B., "Kinetics of oxidation in the Mo-Si system," Aeronautical Systems Div. ASD-TDR-62-203, Part I (May 1962).

[5] "Coatings for refractory metals in aerospace environments," Air Force Contract AF 33(657)-11150, Lockheed Missiles and Space Co., 3rd Quart. Progr. Rept. LMSC 2-04-64-1 (April 1963).

[6] Perkins, R. A., Riedinger, L. A., and Sokolsky, S., "Oxidation protection of refractories during re-entry," Space/Aeronautics **39**, 107–115 (June 1963).

[7] "Evaluation of coatings for refractory metals in aerospace environments," Air Force Contract AF 33(657)-11150, Lockheed Missiles and Space Company, 1st Quart. Progr. Rept. LMSC 2-04-63-1 (September 1963).

JULY-AUG. 1965 J. SPACECRAFT VOL. 2, NO. 4

Low-Density, Autorotating Wings for Manned Re-Entry

H. SCHUERCH*
Astro Research Corporation, Santa Barbara, Calif.

A number of structural and aerodynamic concepts for centrifugally deployed, variable-geometry atmospheric entry aids are discussed. These include means for controlling apex angle of centrifugally stabilized conical flight bodies, the concept of isothermal flight, i.e., atmospheric entry at constant surface temperature, and analytical design of optimum rotor-blade structures. Materials for flexible rotor construction are reviewed and classified according to a temperature-strength parameter that is characteristic for the intended application. Several aerodynamic rotor models subject to qualitative tests are described. An application of the entry rotor concept to a Mars and Earth landing capsule is presented in the form of a conceptual design configuration.

Nomenclature

A = area, ft²
c = chord width, ft
D = drag, lbf
f = Gazley's total energy fraction
$\mathfrak{F}$ = optical view factor
g = gravitational acceleration, ft/sec²
g_c = gravitational acceleration on earth surface, 32.2 ft/sec²
I_p = probability function
$J_{(R,\,\Omega)}$ = auxiliary integral function
l = blade length, ft
L = lift, lbf
m = mass, lbm
m' = mass per unit length, lbm/ft
n = load factor
q = dynamic pressure, lbf/ft²
Q = materials strength: radiation temperature parameter, lbf/sec
R = nondimensional radial coordinate
s = stress, lbf/in²
T = axial blade force, lbf
v = velocity, fps
v^* = specific vehicle velocity, fps
β = coning angle
γ = flight-path angle
ϵ = surface emissivity
θ = absolute temperature, °K
λ = specific strength, in.
ρ = material density, lbm/in.³
ρ_a = atmospheric density, slug/ft³
σ = Boltzmann constant, in.-lbf/sec-in.²-°K⁴
ω = rotational speed, rad/sec
Ω = nondimensional tip speed-to-stress ratio

Introduction

ATMOSPHERIC entry and planetary landing of spacecraft are usually considered in view of fixed-geometry flight configurations with relatively high (≫1 lb/ft²) ballistic parameters.[1] Such configurations emerged from development of ballistic missiles, which, in many respects, were the forerunners of the current generation of space vehicles.

In recent years, various deployable and variable-geometry configurations have been studied[2–5] including inflatable wings, paragliders, variable drag brakes and "rotochutes." In these techniques, large, lightweight surfaces are deployed for aerodynamic control of atmospheric entry. Operational advantages of deployable, variable-geometry configurations include the following: 1) their low ballistic parameters (≤1 lb/ft²) materially reduce heating rates and prolong flight time, thus simplifying both heat protection and flight-path control aspects of manned atmospheric entry, and 2) variable geometry adds a means of control that permits selection of survivable entry trajectories from those initial entry conditions (hyperbolic velocities and steep entry angles) that

Presented at the Engineering Problems of Manned Interplanetary Exploration Meeting, Palo Alto, Calif., September 30–October 1, 1963 (no preprint number; published in bound volume of preprints of the meeting); revision received September 21, 1964. This work has been performed with the financial assistance of NASA.

* President, Astro Research Corporation. Associate Fellow Member AIAA.

would be catastrophic for fixed-geometry vehicles. Studies of variable-geometry and filamentary structures in space operations[6–8] indicate the merits of centrifugal stabilization mechanisms for deployable surfaces. This paper summarizes some of the aerodynamic and structural concepts that have been developed in the course of an exploratory study of rotary atmospheric entry aids.

Variable-Geometry Rotors

The basic configuration selected for study is that of a circular cone with variable apex angle rotating about its axis. This configuration is relatively simple in its aerodynamic and structural characteristics. The structure is considered to be made from thin, flexible material, resistant only in tension. The aerodynamic contour is stabilized and controlled by interactions of aerodynamic and inertial forces. Compact preentry packaging is to be accomplished by folding of the flexible structure. Three principal mechanisms of apex angle variation (Fig. 1) have been considered:

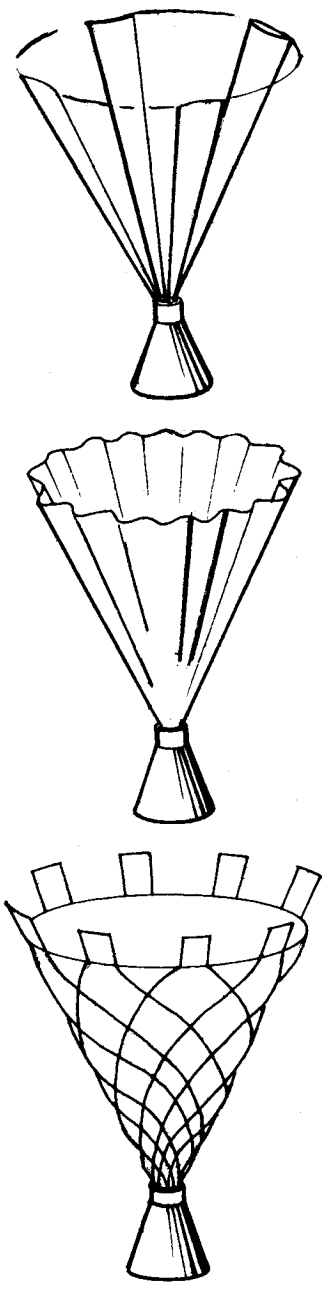

Fig. 1 Variable-geometry rotor configurations.

a) *The leaved cone (or bladed rotor):* If the cone is slit along several meridional lines, it is generic with the well-known helicopter rotor with hinged blades. The "solidity" of the basic configuration and the blade planform shape will determine the coning angle at which the blades will overlap and make the device aerodynamically equivalent to a cone. Variable coning angle requires compliance of the material only at the hub of the rotor and may be effected by localized flapping hinges.

b) *The fluted cone:* If the cone is fluted, the depth of the flutes (or corrugations) will increase as the cone becomes more acute; conversely, at minimum coning it will form a smooth right circular cone (or, in the limit, a flat disk). The material must be compliant in bending (along meridional lines in the circumferential direction only) but may be inextensible in its own plane. The mechanism of deformation is one of metric and topological invariance (isometry), since neither in-plane strains nor cuts are required to allow the geometrical deformation.[8]

c) *A "trellis-shear" deformation:* Here the condition of isometry for the deformed surface is relaxed, since the material is considered as inextensible only along the two directions of two families of threads or filaments. A study of the deformation kinematics of fabric cones shows that a thread geometry forming two counter-rotating sets of logarithmic spirals emanating from the hub will yield the desired apex angle variability of a continuous cone-shaped structure. For this design, a change in coning angle of the structure is associated with a uniform change in the angles formed between the two sets of spirals. (Another configuration[6] involves a somewhat more complicated fiber geometry but provides an invariant fiber stress throughout.)

Isothermal Atmospheric Entry

The structures just described will be flexible membranes made from thin films, fabrics, or thin fiber laminates. As such, they will be incapable of storing appreciable amounts of heat, so that artificial or ablation cooling methods will not be practical. The entry flight duration will be relatively long; the total heat input will be large, but the heating rates will be relatively low. These structures, therefore, will operate essentially at equilibrium temperature (input = radiated output) during the significant portions of the entry deceleration. Assuming that the materials of construction will be able to operate at a given maximum absolute temperature θ, it appears that an "optimum braking trajectory" can be defined for which this temperature is uniform throughout the surface and essentially constant throughout the significant portions of the atmospheric flight path. A vehicle operation that satisfies these conditions of uniform and constant surface temperature will be designated as *isothermal atmospheric entry.*

To define the conditions of configurational and flight-path control required to achieve isothermal flight, consider a vehicle in unpowered flight through the atmosphere of a stationary planet (Fig. 2). Considering equilibrium in directions tangential and normal to the flight path yields, respectively,

$$m(dv/dt) - mg\sin\gamma + D = 0 \tag{1}$$

$$mv(d\gamma/dt) - mg\cos\gamma + L + v^2\cos\gamma/(H + H_0) = 0 \tag{2}$$

Equation (1) can be written in terms of energy rates as follows:

$$d(mv^2/2)/dt + g(dH/dt) + Dv = 0 \tag{3}$$

The third term in Eq. (3) describes the rate at which energy is lost by dissipation. A portion of this power will be transferred to the vehicle in the form of heat; the remainder will appear in the wake as turbulence and heat.

Following Gazley's notation,[1] the heat transferred to the vehicle is expressed as a fraction f of the total energy dissipation. For a given body geometry, f is a function of altitude,

as shown in Fig. 3, which is reproduced from Ref. 1. For altitudes where free molecular flow exists, the fraction f assumes a value of 0.5, i.e., half of the dissipated energy is transferred to the vehicle, the other half is transferred to the wake (equiparation). For equilibrium, the rate at which energy is transferred to the vehicle must equal the rate at which it is radiated from the surface, thus

$$Dvf = \sigma\epsilon\theta^4 A \mathfrak{F} \quad (4)$$

where $\mathfrak{F}$ is a "view factor" that relates the effective radiating surface to the vehicle surface. For an obtuse cone, approaching a flat disk, $\mathfrak{F}$ will approach 2, since both sides of the thin structure will be at the same temperature and will radiate, whereas only the frontal side is subject to heat input.

Substituting Eq. (4) into Eq. (1) and regrouping yields

$$(dv/dt)/g - \sin\gamma = v^*g_c/vfg \quad (5)$$

where g_c is a reference gravitational acceleration of 32.2 ft/sec^2 (earth surface), and

$$v^* = \sigma\epsilon\theta^4 \mathfrak{F} A/g_c m$$

is a *specific velocity*, characteristic of the vehicle's ability to decelerate by rejecting energy from the given area A.

Equations (5) and (2) may be integrated for any given initial condition and lift program, provided that $\mathfrak{F}$ is known. This allows one to establish generalized isothermal trajectory plots. From these the control demands can be derived in terms of drag and/or lift requirements for specific atmospheric density variations. Two simple cases have been considered in some detail: zero-lift, pure-drag modulation; and constant-drag-area, pure-lift modulation.

Drag Modulation

Drag modulation can be accomplished by adjusting the coning angle β measured between the plane normal to the cone axis and the cone meridian. This controls the frontal area to provide the required drag at the instantaneous velocity and altitude. A simple means of control for β consists of a rotor-speed-control device, which provides the centrifugal-force components required to equilibrate the coning moments resulting from aerodynamic pressure forces and axial rotor inertia forces.

For the purpose of this exploratory study, it was assumed that $\mathfrak{F} = 1.0$ and $\epsilon = 0.9$. At the flight conditions H_0, V_0, and γ_0, the vehicle will deploy the cone into essentially a flat disk. The trajectory is then computed for this fixed drag geometry until the desired absolute surface equilibrium temperature θ is reached. At this point, the coning-angle control is assumed to become effective, such that the subsequent portion of the trajectory becomes isothermal. After deceleration to a low velocity, the coning angle required to maintain isothermal flight decreases again to zero. Finally, a constant-area configuration may again be assumed for terminal flight at subsonic equilibrium glide velocity.

The drag is assumed to be

$$D = A \rho_a v^2 \cos^3\beta \quad (6)$$

Table 1 Mars atmospheres

	H.A.E.[1]	Alt. 1	Alt. 2
Inverse scale height, ft^{-1} × 10^5	1.1	1.869	4.506
Surface conditions			
Pressure, *mb*	112	30	11
Density, slug/ft^3 × 10^5	20	9.54	4.21
Temperature, °R	...	414	468
Tropopause altitude, kft	0	0	82.3
Temperature lapse rate, °R/ft × 10^3	0	0	2.84
Chemical composition	N_2	A, CO_2	A, CO_2
Molecular weight	28	44	44

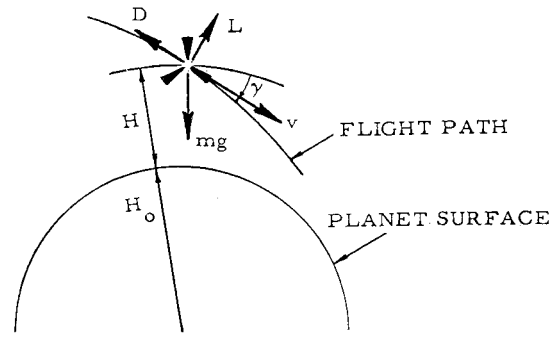

Fig. 2 Atmospheric entry forces.

Reference 11 was used for Earth atmospheric data. Exponential density-altitude variations have been assumed for Mars atmospheres. In addition to the Mars atmosphere from Ref. 1, two alternate atmosphere models were considered in order to explore the range of sea-level density which is more nearly in accord with recent findings (Table 1). The three assumed atmospheres for Mars are believed to cover the range of current assumptions, from most dense (112 *mb* surface pressure) to most tenuous (11 *mb* surface pressure); for these atmospheres, the energy fraction f was assumed to be dependent on atmospheric density only.

A number of typical entry trajectories for Earth and Mars are shown in Figs. 4 and 5. These were selected for entry conditions varying from circular-orbit decay to straight-in entry with parabolic velocity and with specific velocities ranging from 20,000–80,000 fps. The isothermal portion of each trajectory is shown as a solid line. The initial and final flight phases, where the surface temperature is lower than the maximum permitted by the design, are shown as dotted lines. Note that the "high v^*" Mars trajectories never become isothermal, i.e, the cone will remain fully deployed as a flat disk throughout the trajectory, and the vehicle's operation is not temperature-limited. (Trajectories for Venus, not shown, were found to be very similar in character to those for Earth).

Several restrictions will occur in practice for specific applications. These involve the coning-angle requirement, which is subject to practical limitations. Also, for coning angles higher than 45°, the underlying assumptions for drag and heat transfer would need to be modified. Finally, for manned operation, the permissible trajectory deceleration needs to be limited to a value somewhat below 10 Earth g's. In practice, the drag-area control mode would need to be adapted to stay within those limits, and the practicality of the individual trajectory will have to be assessed in view of these limitations.

Lift Modulation

Lift modulation can be accomplished in trimmed flight by variation of incidence angles between rotor axis and flight

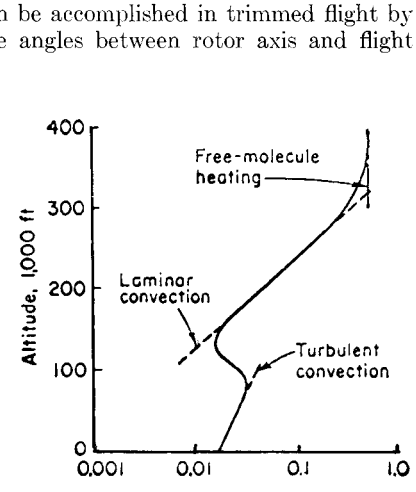

Fig. 3 Energy-conversion fraction.

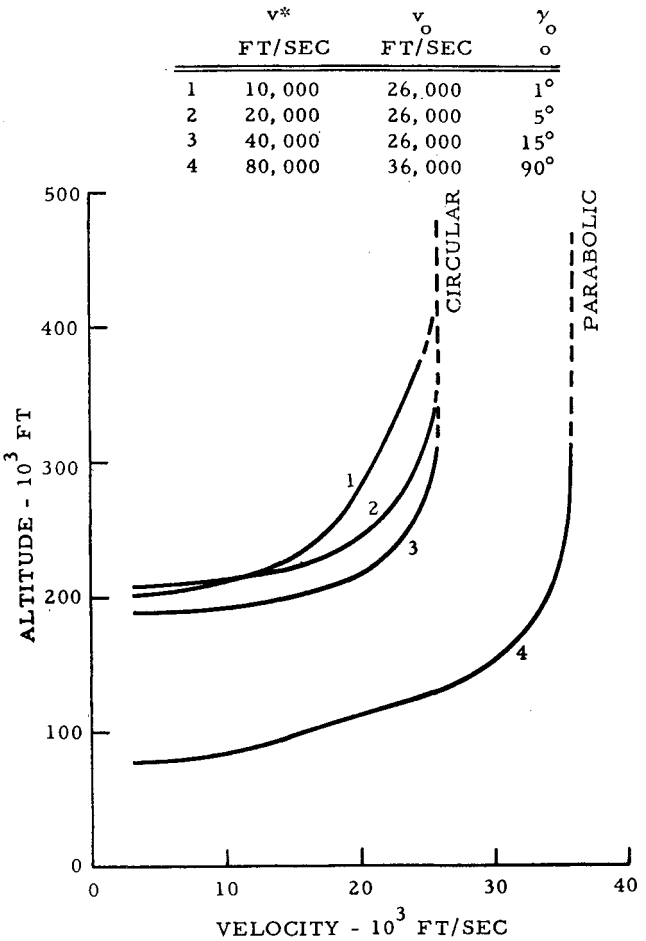

Fig. 4 Drag-modulated trajectories (Earth).

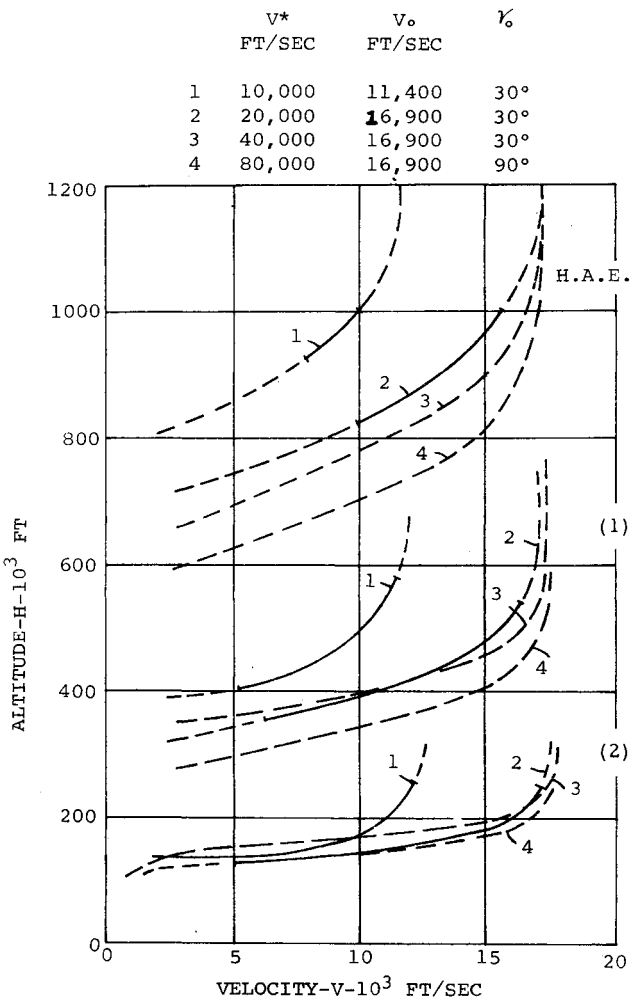

Fig. 5 Drag-modulated trajectories (Mars).

path. Means of accomplishing trim at finite angles of attack are discussed in Ref. 12. For the purpose of trajectory analysis, it was assumed that the coning angle and drag would remain constant. Isothermal flight is then achieved by holding the altitude at which the desired equilibrium temperature is reached until the vehicle decelerates sufficiently to allow descent into denser atmospheric strata. This defines the flight-path angle γ as a function of altitude. The required lift then can be obtained from Eq. (2). It is assumed that the vehicle enters the atmosphere tangentially, i.e., $\gamma = 0$. The relations between v, γ, and required lift vs altitude on Earth entry are shown in Fig. 6 for a vehicle with $v^* = 20{,}000$ fps, assuming again that $\mathfrak{F} = 1.0$ and $\epsilon = 0.9$.

For the particular set of conditions selected, it is seen from Fig. 6 that negative lift is required thoughout the major portion of the flight in order to prevent re-exit of the vehicle due to its supercircular velocity at high altitude. Entry velocities of 40,000 fps for a vehicle with $L/D_{\max}$ capability of -1 are shown to be possible for Earth entry. A "nose-over" condition, requiring large negative lift, is indicated toward the end of the isothermal flight phase. In practice, this maneuver would not be required, but rather a normal glide at reduced surface temperature would be followed.

Analytical Design of Bladed Rotors

For an optimum flexible rotor blade, two conditions need to be satisfied simultaneously: 1) the spanwise distribution of cross-sectional area should be such that the radial stress s is uniform throughout the structure (isotensoid construction allows one to exploit completely the potential strength of the blade material), and 2) the slope of the spanwise blade axis (local coning angle β) should be such that the local heating rates are uniform.

The following assumptions will be made: 1) the blades are sufficiently slender that the blade stresses are parallel to the blade axis, 2) the mass distribution of the rotor is proportional to the cross section required to carry the axial blade tension, and 3) uniform heating rates are achieved by uniform blade slope (zero meridional curvature).

The forces acting on a blade element of unit differential spanwise length, chordwise width c, and mass/unit length m', rotating with angular velocity, are shown in Fig. 7. It is assumed that the aerodynamic pressure force arises from a complete transfer of the air momentum component perpendicular to the blade axis resulting in a normal pressure of $2q\cos^2\beta$, where q is the freestream dynamic pressure. It is further assumed that blade mass inertia forces due to flight-path accelerations are negligible compared to the centrifugal forces caused by rotation. The equilibrium conditions tangential and normal to the blade axis are then

$$-dT/dr = m'r\,\omega^2 \tag{7}$$

$$2qc\cos^2\beta = m'\,r\,\omega^2\sin\beta \tag{8}$$

Equation (7) can be integrated by considering

$$m' = dm/dl = (dm/dr)\cos\beta \text{ and } T = m'\,s/\rho$$

where ρ is the density, and s is the stress in the blade material, yielding

$$m' = m_H'\exp[-\Omega(R^2 - R_H^2)/2] \tag{9}$$

where m_H' indicates the mass/unit length at the hub radius r_H, $R \equiv r/r_0$, and $R_H \equiv r_H/r_0$ are nondimensional coordinates, and $\Omega \equiv r_0^2\,\omega^2\,\rho/s$ is a nondimensional rotational frequency, characteristic of the blade design.

The mass distribution given by Eq. (9) (and, therefore, the rotor's cross-sectional area) does not vanish at the tip ($R = 1$). Therefore, a concentrated tip mass m_0 is required to satisfy the condition of constant stress:

$$m_0 = (l_0/\Omega)\, m_H' \exp\,[-\Omega(1 - R_H^2)/2] \qquad (10)$$

This will normally be a small fraction of the total rotor mass.

From Eq. (8), a relation between the chord distribution and mass distribution is derived that satisfies the condition of uniform coning angle:

$$c = c_{REF}\, R \exp\,[-\Omega(R^2 - R_H^2)/2] \qquad (11)$$

where the reference chord width is defined by

$$c_{REF} = m_H'\, l_0 \frac{\omega^2 \tan\beta}{2q} = \frac{A\Omega}{l_0}\left\{1 - \exp\left[\frac{-\Omega\,(1 - R_H^2)}{2}\right]\right\}^{-1}$$

Figure 8 shows nondimensional plots of the mass and chord distribution of rotor blades satisfying the condition of uniform stress and coning angles for a number of selected values of the nondimensional rotational speed.

The distributed rotor mass is obtained by integrating Eq. (9). The result can be expressed in terms of the tabulated probability function,

$$I_{p(x_1)} = \frac{2}{\pi^{1/2}} \int_0^{x_1} e^{-x^2}\, dx$$

as

$$m_R = m_0 + m_H'\, l_0 \Omega^{-1/2} J_{(R_H,\,\Omega)} \qquad (12)$$

where

$$J_{(R_H,\,\Omega)} = (\pi/2)^{1/2} e^{\Omega R_H/2}\, I_{p(\Omega/2)^{1/2} - I_{p[(\Omega/2)^{1/2} R_H]}}$$

For practical values of Ω and R_H, the expression $J_{(R_H,\,\Omega)}$ will approximately equal $(\pi/2)^{1/2}$. The resultant force F_H parallel to the rotor axis, which is imparted to the payload m_P, is equal to the required trajectory deceleration, given in terms of Earth gravity g_c:

$$F_H = T_H \sin\beta = m_H\,(s/\rho)\,\sin\beta = m_P(n g_c)$$

This permits computation of the relative mass fraction between the mass m_R of an ideal rotor and the payload mass m_P:

$$\frac{m_R}{m_P} = n\, \frac{l_0(SF)}{\lambda_{sp} \sin\beta}\, \frac{J_{(R_H,\,\Omega)}}{\Omega^{1/2}\,(1 - m_0/m_R)} \qquad (13)$$

where λ_{sp} is the specific strength of the rotor material, and (SF) is the ratio of ultimate tensile strength to working stress (safety factor) employed in the rotor design. Note that the rotor mass fraction is a linear function of absolute size l_0. This is an expression of the "square-cube law" well known in aircraft design.

With some transformation, Eq. (13) can be written as

$$\frac{m_R}{m_P} = n\, \frac{[J_c(SF)/\omega^2 \lambda_{sp}]^{1/2}}{\sin\beta\, \cos\beta}\, \frac{J_{(R_H,\,\Omega)}}{1 - m_0/m_R} \qquad (14)$$

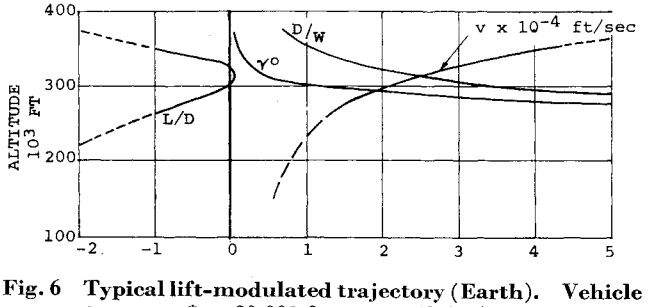

Fig. 6 Typical lift-modulated trajectory (Earth). Vehicle parameters are $v^* = 20{,}000$ fps, $\beta = 45°$, W/A = 0.2 lb/ft², $\theta = 780°$C.

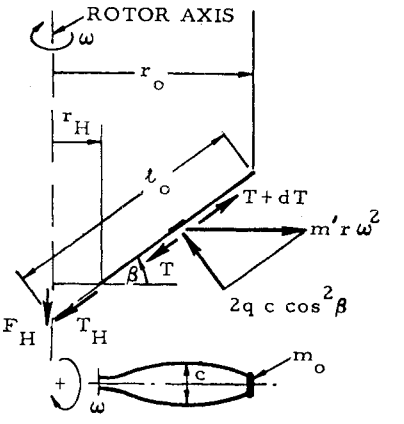

Fig. 7 Rotor blade forces.

The rotor mass fraction is inversely proportional to the rotational frequency. Since rotor stress is a direct function of tip speed, the rotor efficiency again is penalized by size.

Introducing reasonable values for a series of rotors with a payload capability of 3000 lb, the rotor structural mass fraction is found to range between 1 and 5%. For instance, let the designing condition of an entry condition be $n = 10$, $\beta = 45°$. Assume the rotor to be designed to rotate at $\omega = 10$ rad/sec, to be made from a material with $\lambda_{sp} = 0.5 \times 10^6$ in., and to be designed with $SF = 2$. For these values, the ideal structural rotor weight fraction becomes approximately 2%.

In many instances, the weight of the rotor will not be determined by strength considerations, but by considerations of minimum practical material thickness at the rotor tips. In this case, the "constant stress" rotor mass is determined by

$$m_R = A \rho t_{min}\, \Omega^{1/2} J_{(R_H,\,\Omega)} + m_0 \qquad (15)$$

The rotor mass given by Eq. (15) does not necessarily represent a minimum, since gage considerations may only affect a portion of the blade area, allowing the stress to be higher at the root than at the tip.

Another consideration is that of distributed rotor masses associated with surface-area covering, in addition to that required by structural strength alone. Such nonstructural parasitic masses affect both the structural mass distribution and the chord distribution of an ideal blade. Analytical design equations (omitted from this paper for the sake of brevity) have been developed for this case.

Materials Selection for High-Temperature Rotors

An extensive effort has been directed, during the past few years, toward the study and development of temperature-resistant, packageable filament- and fabric-type materials, particularly for application in high-speed parachutes, and

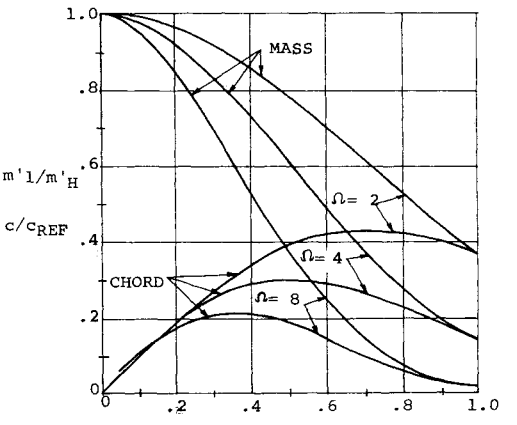

Fig. 8 Chord and mass distribution for ideal rotor blade.

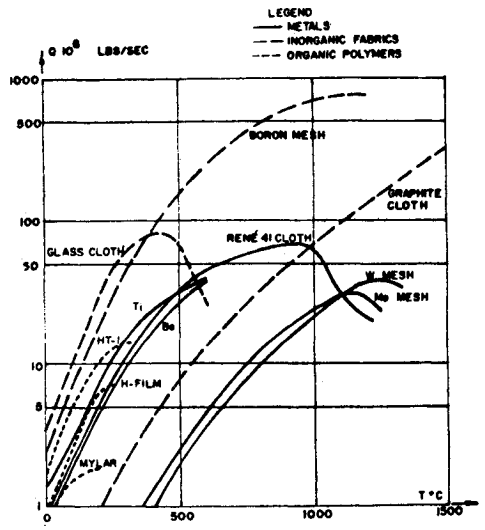

Fig. 9 Material parameter Q vs temperature.

temperature-resistant, filament-wound structures.[9,10] An important rating parameter is the material's ability to maintain a useful tensile strength for a given structural mass while rejecting thermal energy by radiation; this rating parameter can be defined

$$Q \equiv \sigma \epsilon \theta^4 \lambda_{sp}$$

Since both ϵ and λ_{sp} are temperature-dependent, Q will be an empirical function of temperature (θ), normally rising to a maximum value after which the degradation of strength becomes stronger than the increase in radiative power dissipation. In practice, the situation is further complicated by the fact that λ_{sp} depends not only on θ, but also on the previous load-temperature history. For the purpose of this discussion, it was decided to compare materials on the basis of their short-term strength-at-temperature characteristics, which may be considered reasonably representative for the intended operation of the rotor configuration during atmospheric entry. Figure 9 shows values of Q for various materials computed from data on λ_{sp} and ϵ collected from numerous sources.

The outstanding potential of elemental boron fibers in the particularly interesting temperature range from 400° to 1200°C is readily apparent from Fig. 9. Since few reliable data were available for this relatively new material, a laboratory setup was constructed to produce experimental quantities of continuous boron filaments. Filaments of approximately 2-mil diam were produced and subjected to tensile tests at temperatures up to 1200°C in an inert atmosphere and in air. In addition, several composites and laminates were made with elemental boron fiber base materials.[13] The test data, as reflected in Fig. 9, generally confirm the exceptional physical properties of this material.

For rotors that can operate at very low v^* (for shallow entry), equilibrium temperatures of 400°C and less appear to be practical. For this application, various types of glass and temperature-resistant synthetic textile fabrics can be considered. For small, highly loaded rotors, which may be required to operate at high v^* (~80,000 fps) for "straight-in" trajectories for planetary entry into nonoxidizing atmosphere, carbon or graphite cloth may be considered.

Experiments

A number of rotor models have been fabricated and subjected to qualitative tests in a low-speed vertical tunnel. The models were designed to represent the three basic configurational control schemes (bladed rotor, fluted cone, and spiral net) discussed previously. The object of the tests was to observe the ability of each model to deploy itself in an axial air stream and autorotate at various coning angles at various angles of flow incidence.

The air-stream velocity in the test section was 14 fps, generating a dynamic pressure of approximately 0.22 psf. The configurations of the model rotors were such that in most cases stalled or near-stalled flow conditions prevailed; thus the aerodynamic characteristics of hypersonic flow were approached at least qualitatively. Characteristic flutter motions in nonmass-balanced blades and deployment dynamics of the various rotor were observed and recorded by motion pictures. Rotational speeds were measured by means of a strobelight, and airspeed by means of a torque vane. No attempt was made to obtain quantitative lift and drag data. It was observed, however, that most rotors would more than support their own weight in axial flow, indicative of normal force coefficients based upon disk area in excess of 1.0.

Figure 10 shows a typical *bladed rotor* made from thin Mylar film, rotating with essentially zero coning angle at approximately 220 rpm and an angle of flow incidence of approximately 70°. It was found that the blade center-of-gravity axis needs to be placed slightly forward of the 25%-chord line to prevent torsion-bending blade flutter. Balancing is accomplished by small lead weights clamped to the leading edge of each blade. The completely flexible rotor is mounted on a bearing-supported hub that can be tilted through a 90° angle during operation. This model deployed automatically and maintained stable autorotation throughout a 70° range of inflow incidence.

Figure 11 shows a *fluted cone* model made of Dacron fabric. Tip weights are attached to short chain links at each seam of the convoluted configuration. The convolutions are tailored to form a spiral groove, which causes the configuration to be driven into rotation by the axial air stream. Automatic deployment at low axial-flow velocities was achieved, but sig-

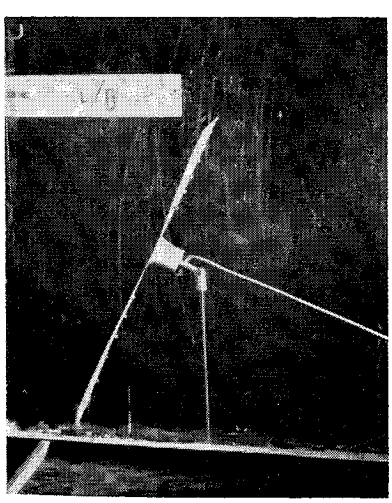

Fig. 10 Mylar film blade in autorotation at incidence angle of 70°.

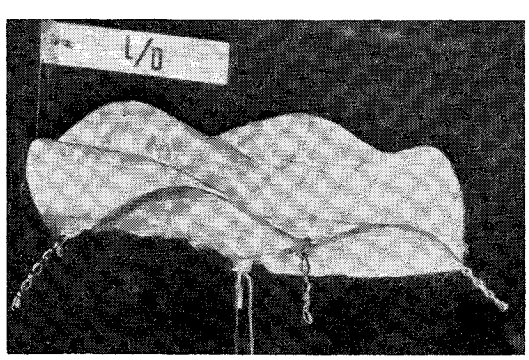

Fig. 11 Fluted cone in axial flow.

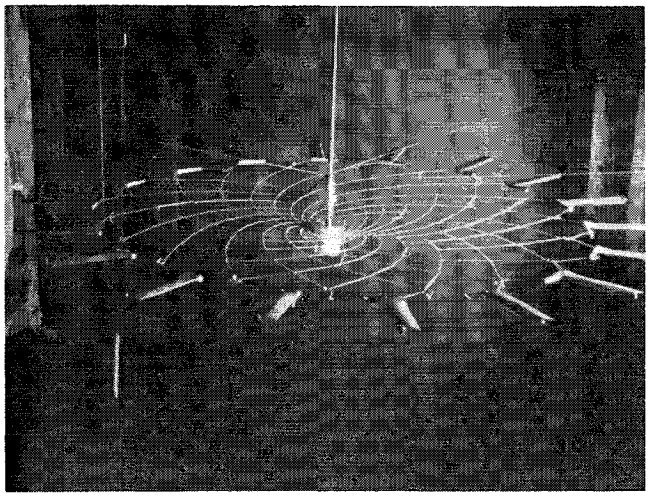

a) Open mesh with tip impellers.

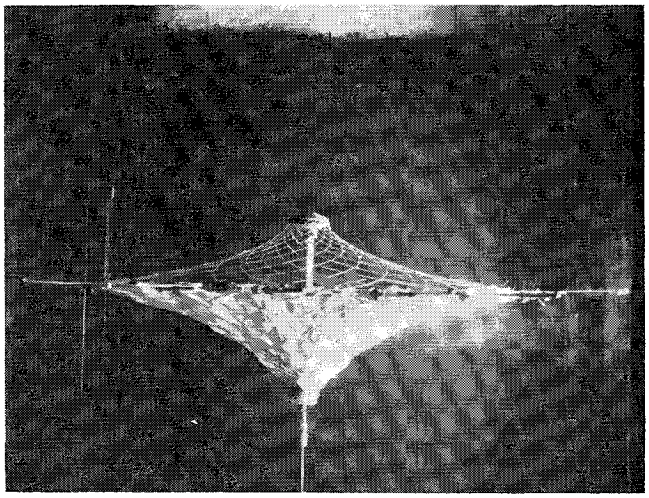

b) Composite, open mesh plus aerodynamic cover.

Fig. 12 Spiral net rotor.

nificant angles of incidence could not be maintained with this model.

An *open-mesh, spiral-net* model in axial flow is shown in Fig. 12a. Autorotation is maintained by impeller tabs fastened to the periphery of the net. Tilting of the hub axis did not affect the rotor's tendency to be oriented with its plane normal to the air stream. The same net was tested with an aerodynamic covering. Both configurations deployed automatically and maintained stable rotation through a range of coning angles. A composite configuration of two nets mounted with hubs spaced by a shaft is shown in Fig. 12b. The upper net is open, but the lower net is covered to provide

Table 2 Design characteristics for Mars entry vehicle

Characteristics	Measurements
Total mass	2000 lb
Rotor area	10,000 ft^2
v^*	20,000 fps
Q	0.33×10^9 lb/sec
Maximum deceleration	10 g_c
Blade parameter, Ω	4
Blade length, l_0	135 ft
Temperature	760°C
Design safety factor	2
Structural weight of ideal rotor	43.7 lb
Tip weights (total of 8)	2.4 lb

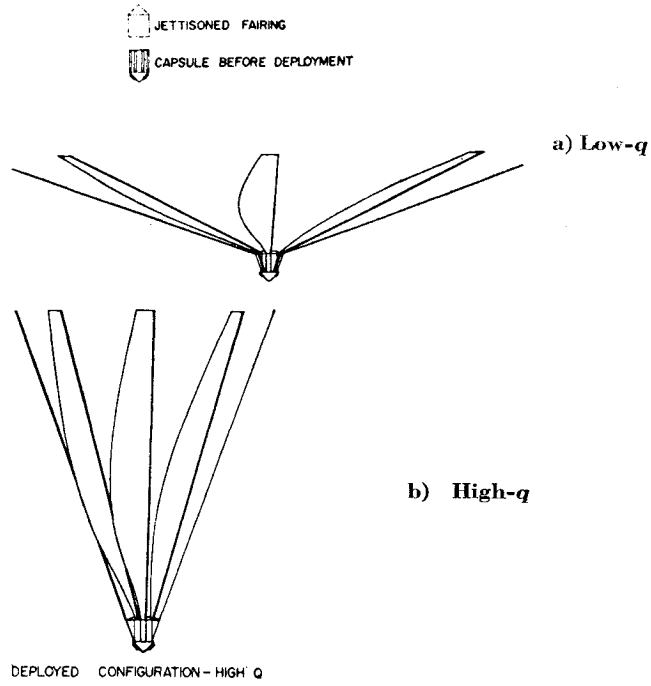

Fig. 13 Bladed-rotor deployment configurations.

an aerodynamic surface. Coning-angle control of this configuration proved capable of maintaining stable rotation at incidence angles up to approximately 45°.

Applications

A number of mission profiles (as reflected by the trajectory requirements) have been studied with respect to the design configurations required. A conceptual design is shown in Fig. 13 for a vehicle capable of Mars entry with an initial flight-path angle of 30° from parabolic velocity and return into Earth's atmosphere with an initial path angle of 5° from circular orbit. Figure 13a shows a deployed low-q configuration such as would be used for the initial entry and terminal flight phase; Fig. 13b shows the high-q configuration required at maximum deceleration with a coning angle of 70°. Some

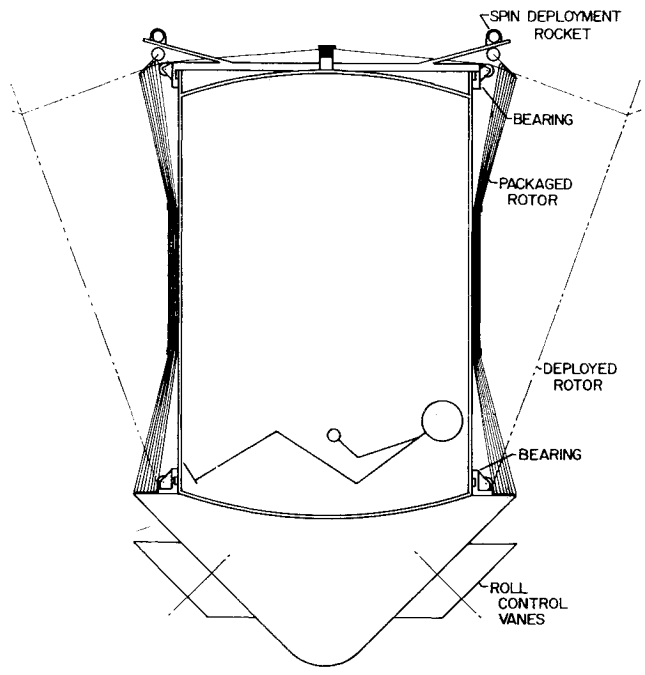

Fig. 14 Packaged rotor and capsule concept.

details of the capsule arrangement with the packaged rotor are shown in Fig. 14.

The design characteristics selected for this vehicle are shown in Table 2. The structural requirements for the particular configurat on selected leads to extremely low blade thickness (1.3 mil at the root). Thus, it would be expected that a "practical" design will employ a heavier rotor by perhaps a factor of 5. Even if this penalty is accepted, the payload mass fraction would appear to compare favorably with ablation-protected entry capsules. It points, however, to the desirability of developing extremely thin, heat-resistant fabric and film materials for this application.

References

[1] Koelle, H. (ed.), *Handbook of Astronautical Engineering* (McGraw-Hill Book Co., Inc., New York, 1961), Chap. 10, pp. 5, 24.

[2] Slivka, L. P., "Development of pneumatic structural material for helicopter rotor blades," Goodyear Aircraft Corp., Rept. GER-7236 (January 1956).

[3] Wornom, D. E. and Taylor, R. T., "Aerodynamic characteristics of a flexible-canopy paraglider model at a Mach number of 4.5 for angles of attack to 360° and sideslip angles from 0° to 90°," NASA TN D-1776 (April 1963).

[4] Alexander, W. C., "Investigation to determine the feasibility of using inflatable balloon type drag devices for recovery applications in the transonic, supersonic, and hypersonic flight regime—part II: Mach 4 to Mach 10 feasibility investigation," Goodyear Aircraft Corp., Aeronautical Systems Div. ASD-TDR-62-702, Pt. II (December 1962).

[5] Packard, C. B., "Final Report of KRC-4 Rotochute Development," Kaman Aircraft Corp., Rept. R-239 (August 1958).

[6] Kyser, A. C., "The uniform-stress spinning filamentary disk," Astro Research Corp., Rept. ARC-R-150 (May 1964).

[7] Burggraf, O. and Schuerch, H., "Analysis of Axisymmetric, Rotating Pressurized Filamentary Structures," Astro Research Corp., NASA TN D-1920 (May 1963).

[8] Schuerch, H. and Schindler, G., "A contribution to the theory of folding deformations in expandable structures with a particular application to toroidal shells," Astro Research Corp., NASA TN D-1690 (December 1962).

[9] Coplan, M. J., Freeston, W. D., and Powers, D. H., "Flexible, low porosity, woven metallic materials," Fabric Research Labs., Inc., Aeronautical Systems Div. ASD-TR-61-677 (November 1961).

[10] Kolarik, R. V. and Marco, D. M., "New and improved materials for expandable structures—Phase IV—High temperature protective study," Goodyear Aircraft Corp., Aeronautical Systems Div. ASD-TDR-62-542, Pt. V (February 1963).

[11] *U. S. Standard Atmosphere—1962*, (U. S. Govt. Printing Office, Washington, D. C., 1962); prepared under sponsorship of NASA, U. S. Air Force, and U. S. Weather Bureau.

[12] MacNeal, R., "Deployable centrifugally stabilized structures for atmospheric entry from space—Part II: hypersonic rotor dynamics," Astro Research Corp., Rept. ARC-R-104 (August 1963).

[13] Witucki, R., "Boron filaments," Astro Research Corp., Rept. ARC-R-107 (September 1963).